Asociación Argentina
de Mecánica Computacional

Mecánica Computacional Vol XXXIII, págs. 129-145 (artículo completo)
Graciela Bertolino, Mariano Cantero, Mario Storti y Federico Teruel (Eds.)
San Carlos de Bariloche, 23-26 Setiembre 2014

TRIBOLOGICAL PERFORMANCE OF TEXTURED SURFACES IN THE PISTON RING/LINER CONTACT USING THE ELROD-ADAMS MODEL

Hugo M. Checo[a], Alfredo Jaramillo[a], Mohammed Jai[b] and Gustavo C. Buscaglia[a]

[a]*Inst. de Ciências Matemáticas e de Computação, Universidade de São Paulo, 13560-970 São Carlos, Brazil, http://http://www.icmc.usp.br*

[b]*Institut Camille Jordan, INSA de Lyon , 69621 Villeurbanne, France, http://http://math.univ-lyon1.fr*

Keywords: Friction reduction, textured surfaces, piston ring, Elrod-Adams model.

Abstract. The possibility of improving the performance of lubricated surfaces through surface texturing has been a topic of intense research in the latest years. Considerable efforts in both experimental and numerical works have been made to study the effects of micro-textures in load capacity, friction and wear. In the industry it has been known for a long time that some texturing is required in the liners of combustion engines to avoid stiction with the piston rings. The numerical simulation of that problem poses a challenge in modeling the intervening phenomena (cavitation, starvation, ring dynamics) and solving it efficiently.

In this work we present numerical simulations of the piston ring/liner problem in the hydrodynamic lubrication regime using the Elrod-Adams model and a mass-conserving algorithm. Realistic values are assumed for the parameters defining the problem. The formation of cavitation bubbles and its relation with the load-carrying capacity, friction and clearance is analyzed by considering different texture configurations and shapes in one-dimensional tests. Afterwards, two-dimensional dimpled surfaces are simulated for more than a hundred different texture configurations in the hydrodynamic lubrication regime for several Stribeck numbers. A robust code accelerated by means of a multigrid implementation allowed the realization of this extensive study. Results show that friction and wear reduction are attainable by virtue of dimples of the size of the contact, although the gain decreases or disappears as the mixed lubrication regime is approached.

1 INTRODUCTION

Modifying the contacting surfaces in lubricated pairs in order to improve its tribological performance has been a long-term practice. In the specific case of cylinder liners of combustion engines the abrasive machining process known as honing is used to generate a cross-hatched finish to ensure proper lubrication, as well as to avoid deleterious effects such as stiction.

The availability of new microengineering techniques such as Laser Surface Texturing (LST) (Etsion (2005)) allowing tailor-made surfaces to be produced, has made the topic of the optimal geometry for a certain application the subject of intensive research in the last years.

There seems to be a general consensus for the beneficial effects of textures (dimples and micro-grooves) in devices such as thrust bearings, where conformal contact (parallel or almost parallel surfaces) is involved. This is shown in Mishra and Polycarpou (2011), Ramesh et al. (2013), Yuan et al. (2011), Wang et al. (2006), Bifeng et al. (2012) and Cho and Park (2011). On the other hand, opposite results have been reported in a few cases (Pettersson and Jacobson (2007); Kovalchenko et al. (2005)).

Some applications, as is the case of the piston ring/liner contact, do not fall in the previous category. In the non-conformal situation, the experimental study of Costa and Hutchings (2007) showed that larger curvature radius in cylinder against textured flat surface tests led to a benefit in texturing, while smaller radii had the opposite effect. Gadeschi et al. (2012) studied the effect of the curvature on minimum film thickness, load capacity, friction force and friction coefficient for barrel shaped textured rings using the Reynolds equation with Gümbel boundary condition for cavitation. Similar conclusions were reached: for large ring curvatures the textured cases would perform worse than their untextured counterparts, and vice-versa. These findings are also supported by Kovalchenko et al. (2011), Ali et al. (2012), Tomanik (2008) and Dobrica et al. (2010).

Most works addressing textured surfaces in the piston ring/liner problem consider the textures on the ring (Etsion and Sher (2009); Qiu and Khonsari (2011); Gadeschi et al. (2012)). It seems preferable to put textures on the liner instead of the ring, as textures on the ring are expected to last only the break-in period. LST on the bore is expected to last the engine lifetime (Tomanik (2013)). Besides, this also allows to texture only selected parts of the engine cycle.

Few numerical works (Organisciak and Cavallaro (2005); Tomanik (2013)) consider textures on the liner, and even fewer contemplate that the dynamical behavior of the ring must be taken into account (Buscaglia et al. (2010); Checo et al. (2014)). Textures on the ring are stationary and thus the ring reaches a equilibrium position, stabilizing at the point where equilibrium of forces take place. When textures are set on the liner they are moving through the domain. The passing of a texture under the ring causes a oscillatory motion, hence the simulation must be transient in this case, incorporating the rigid-body dynamics.

In this article, the piston ring/liner problem with textures on the liner will be addressed, taking into account the ring dynamics. The mass-conserving Elrod-Adams model (Elrod and Adams (1974)) is used to model cavitation in lubrication. Mass-conservation has been proven numerically (Ausas et al. (2009a)) and experimentally (Zhang and Meng (2012)) to be essential to achieve meaningful physical results. Although the piston velocity and loads on the rings vary along an engine cycle, constant values for those parameters are considered, corresponding to those of mid-stroke of a four-stroke combustion engine. Only the hydrodynamic lubrication regime is studied, by imposing a sufficiently low load on the ring.

This paper is organized as follows: in Section 2 the mathematical model is described. Section 3 presents the numerical method. A finite volume discretization is employed to solve the Elrod-Adams model, with convergence acceleration through a multigrid method. Multigrid performance results as well as mesh-converged numerical simulations for one and two-

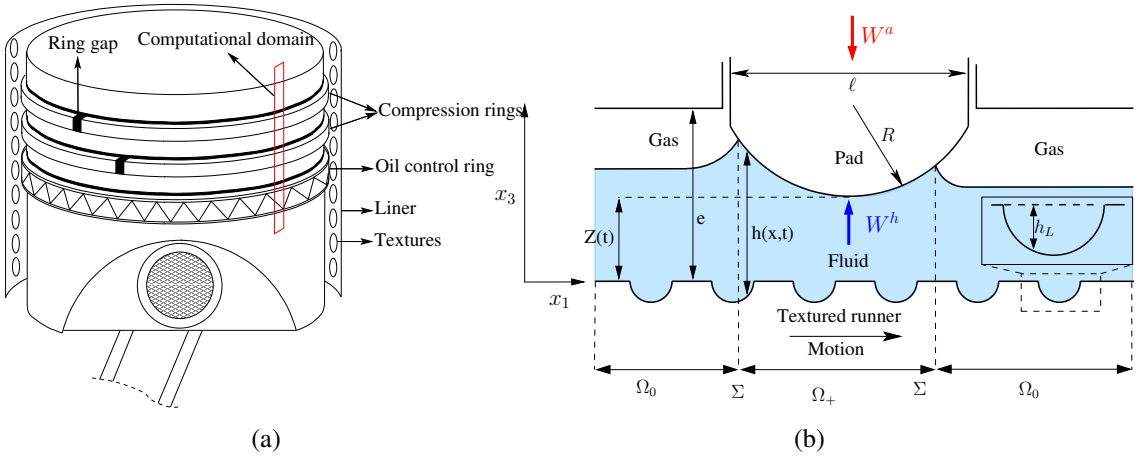

Figure 1: Figure (a) shows a scheme of a ring pack placed in the piston. The computational domain is bounded by a red rectangle while figure (b) depicts a section along the piston's direction of motion, with the forces acting on it.

dimensional textures are shown and discussed in Section 4. The former set of tests (one-dimensional) thoroughly explores sinusoidal textures for two ring curvature radius and fixed velocity and loads on the ring. The latter considers dimples with dimensions inspired in those produced by LST for 10 ring curvature radius, from 2 mm to 1024 mm. Finally, conclusions are drawn in Section 5.

2 MODEL

A very thin stripe of the liner surface in the piston movement direction is chosen as the computational domain, which is shown in fig. 1. The direction of the motion of the piston is chosen to be x_1, while the runner is assumed to coincide with the $x_1 - x_2$ plane. The frame of reference is fixed on the ring and thus we assume that the liner moves with velocity u (the piston is moving with velocity $-u$ in a frame attached to the liner).

Textures on the liner are given by a function $x_3 = -h_L(x_1, x_2) \leq 0$ ($h_L(x_1, x_2)$=0 for the untextured liner). They are periodic in both x_1 and x_2 directions, therefore $0 < x_2 < w$, with w large enough to contain one texture period. In the x_1 direction the domain extent is $x_\ell < x_1 < x_r$.

A single ring of length ℓ is considered with profile $h_U(x_1, x_2)$ satisfying $\min_{(x_1,x_2)} h_U(x_1, x_2) = 0$. Its analytical expression corresponds to an arc of circumference of radius R located in $x_\ell < a \leq x_1 \leq b < x_r$. A uniform thickness e is assumed outside the pad's location. Hence, we have for the gap between the liner and the ring:

$$h(x_1, x_2, t) = \begin{cases} h_L(x_1 - u\,t, x_2) + h_U(x_1, x_2) + Z(t) & \text{if } a < x_1 < b \\ h_L(x_1 - u\,t, x_2) + e & \text{otherwise} \end{cases} \tag{1}$$

where $Z(t)$ denotes the vertical distance between the pad and the $x_1 - x_2$ plane.
Besides the geometrical features we also need to model:

1. The fluid dynamics,

2. The ring dynamics (forces acting on it).

2.1 Thin film fluid dynamics with cavitation

The very thin gap between the ring and liner allows the use of the lubrication approximation (Reynolds equation). Due to the convergent-divergent geometry of the ring/textured liner contact and to the movement of the ring in its placement cavitation takes place. In this work we adopt the well-known Elrod-Adams model (Elrod and Adams (1974)) which incorporates into a single formulation the Reynolds equation for the pressurized region and the Jacobsson-Floberg-Olsson boundary conditions for cavitation. Comparison between results with this mass-conserving model and experiments show excellent agreement (Zhang and Meng (2012)).

The model postulates the computation of two fields, p and θ, which correspond to the hydrodynamic pressure and to an auxiliary saturation-like variable, respectively, that (weakly) satisfy the equation

$$\nabla \cdot \left(\frac{h^3}{12\mu} \nabla p \right) = \frac{u(t)}{2} \frac{\partial\, h\theta}{\partial x_1} + \frac{\partial\, h\theta}{\partial t} \tag{2}$$

under the complementarity conditions

$$\begin{cases} p > 0 & \Rightarrow \quad \theta = 1 \\ \theta < 1 & \Rightarrow \quad p = 0 \\ 0 \leq \theta \leq 1 \end{cases} \tag{3}$$

where μ is the viscosity of the lubricant.

Initial conditions for θ and p are provided. A constant film thickness of lubricant d_{lub} is assumed upstream of the ring, which amount to imposing $\theta = d_{\text{lub}}/h$ at the boundary of the computational domain. At $x_2 = 0$ and $x_2 = w$ proper boundary conditions are set to enforce periodicity in the x_2 direction.

At each instant the domain spontaneously divides into a *pressurized* region, Ω^+, where $p > 0$, and a *cavitated* region, Ω^0, where the film is not full ($\theta < 1$, see figure 1). At the boundary between Ω^+ and Ω^0, the so-called cavitation boundary Σ, the Elrod-Adams model automatically enforces mass-conservation.

2.2 Ring dynamics

Several forces act on the ring in the x_3 direction. Here we focus in two of them:

1. The *pre-stress force* W^a: pointed downwards (i.e.; along $-x_3$) and is assumed constant. Comes from the elastic response of the ring to the deformation needed to fit its placement;

2. The *hydrodynamic force* W^h: originates from the pressure $p(x_1, x_2, t)$ that develops in the ring/liner bearing:

$$W^h(t) = \frac{1}{w} \int_0^w \int_a^b p(x_1, x_2, t)\, dx_1\, dx_2 \tag{4}$$

Notice that this two forces are forces per unit width. Other two relevant forces acting on it are the contact force due to interaction between the surface's asperities and the one coming from pressure of the combustion gases acting on the back part of the ring. Only constant loads on the ring in the hydrodynamic lubrication regime will be assessed in this work, and hence these last two forces won't be considered.

We assume no tilting of the ring and then the ring dynamics is given by Newton's second law in the x_3 direction:

$$m\frac{d^2Z}{dt^2} = -W^a(t) + W^h(t) \tag{5}$$

where m is the ring's linear mass. This is supplemented with initial conditions for Z and Z' at $t = 0$.

2.3 Non-dimensionalization

Three fundamental scales are chosen:

- U for velocity;
- L for lengths in the $x_1 - x_2$ plane and also for R;
- H for lengths in the x_3 direction.

Their values are set to U=10 m/s, $L = \ell$= 10^{-3}m (equal to the ring's length) and H= 1 μm. The lubricant viscosity is set to μ= 0.004 Pa.s A detailed description of the non-dimensionalization can be seen in Checo et al. (2014).

Upon non-dimensionalization of all variables (non-dimensional variables will be kept from this point on), the complete non-dimensional mathematical problem to be solved reads:

"Find trajectory $Z(t)$, and fields $p(t)$, $\theta(t)$, defined on $\Omega = (x_\ell, x_r) \times (0, w)$ and periodic in x_2, satisfying

$$\begin{cases} Z(0) = Z_0, \qquad Z'(0) = V_0, \\ \theta(x_\ell, x_2, t) = d_{\text{lub}}/h(x_\ell, x_2, t) \qquad \forall x_2 \in (0, w) \\ p > 0 \qquad \Rightarrow \qquad \theta = 1 \\ \theta < 1 \qquad \Rightarrow \qquad p = 0 \\ 0 \leq \theta \leq 1 \end{cases} \tag{6}$$

and

$$m\frac{d^2Z}{dt^2} = -W^a + W^h(t) \tag{7}$$

$$\nabla \cdot \left(h^3 \nabla p\right) = u\,\frac{\partial\, h\theta}{\partial x_1} + 2\frac{\partial\, h\theta}{\partial t} \tag{8}$$

where

$$h(x_1, x_2, t) = \begin{cases} h_L(x_1 - u\,t, x_2) + h_U(x_1, x_2) + Z(t) & \text{if } a < x_1 < b \\ h_L(x_1 - u\,t, x_2) + e & \text{otherwise} \end{cases}, \tag{9}$$

$$W^h(t) = \frac{1}{w}\int_a^b \int_0^w p(x_1, x_2, t)\, dx_1\, dx_2\,, \tag{10}$$

and the functions $h_L(x_1, x_2)$ and $h_U(x_1, x_2)$ are known explicitly."

3 NUMERICAL METHOD

A finite volume, mass-conserving method with upwinding discretization of the Couette flux and centered discretization of the Poiseuille flux is employed in a cartesian mesh to solve equation (8), as done by Ausas et al. (2009a). The rectangular domain $\Omega = (x_\ell, x_r) \times (0, w)$ is

divided in $N_1 \times N_2$ cells ($\Delta x_1 = \frac{x_r - x_\ell}{N_1}$, $\Delta x_2 = \frac{w}{N_2}$). The adopted finite volume discretization of the Elrod-Adams equation is:

$$2\Delta x_1^2 \frac{c_{i,j}^n - c_{i,j}^{n-1}}{\Delta t} + U^n \Delta x_1 (c_{i,j}^n - c_{i-1,j}^n) = s_{i,j}^n p_{i+1,j}^n - (s_{i,j}^n + s_{i-1,j}^n) p_{i,j}^n + s_{i-1,j}^n p_{i-1,j}^n + q^2 [s_{i,j+1}^n p_{i,j+1}^n - (s_{i,j+1}^n + s_{i,j-1}^n) p_{i,j}^n + s_{i,j-1}^n p_{i,j-1}^n] \quad (11)$$

Where:

$$s_{i,j+1} = \frac{h_{i,j}^3 + h_{i+1,j}^3}{2}\,, \qquad c_{i,j} = \theta_{i,j} h_{i,j}\,, \qquad q = \frac{\Delta x_1}{\Delta x_2}$$

The complementarity conditions must be fulfilled:

$$0 \le p_{i,j}^n\,, 0 \le \theta_{i,j}^n \le 1$$

$$p_{i,j}^n > 0 \Leftrightarrow \theta_{i,j}^n = 1$$

i, j designate the position of a cell in the x_1 and x_2 directions, where $i = 1, ..., N_1$ and $j = 1, ..., N_2$. n specifies at which time step the corresponding variable is assessed.

From eq. (11 the following can be obtained:

$$P_{i,j}^{n,k} = \frac{1}{s_{i,j}^{n,k-1} + s_{i-1,j}^{n,k-1} + q^2 (s_{i,j+1}^{n,k-1} + s_{i,j-1}^{n,k-1})} (-2\Delta x_1^2 \frac{c_{i,j}^{n,k-1} - c_{i,j}^{n-1}}{\Delta t} - U^n \Delta x_1 (c_{i,j}^{n,k-1} - c_{i-1,j}^{n,k-1}) + s_{i,j}^{n,k-1} p_{i+1,j}^{n,k-1} + s_{i-1,j}^{n,k-1} p_{i-1,j}^{n,k-1} + q^2 (s_{i,j+1}^{n,k-1} p_{i,j+1}^{n,k-1} + s_{i,j-1}^{n,k-1} p_{i,j-1}^{n,k-1})) \quad (12)$$

$$\Theta_{i,j}^{n,k} = \frac{1}{(\frac{2\Delta x_1^2}{\Delta t} + U^n \Delta x_1) h_{i,j}^{n,k}} (\frac{2\Delta x_1^2}{\Delta t} c_{i,j}^{n-1} + U^n \Delta x_1 c_{i-1,j}^{n,k-1} + s_{i,j}^{n,k-1} p_{i+1,j}^{n,k-1} - (s_{i,j}^{n,k-1} + s_{i-1,j}^{n,k-1}) p_{i,j}^{n,k-1} + s_{i-1,j}^{n,k-1} p_{i-1,j}^{n,k-1} + q^2 [s_{i,j+1}^{n,k-1} p_{i,j+1}^{n,k-1} - (s_{i,j+1}^{n,k-1} + s_{i,j-1}^{n,k-1}) p_{i,j}^{n,k-1} + s_{i,j-1}^{n,k-1} p_{i,j-1}^{n,k-1}]) \quad (13)$$

This is solved for each cell in a Gauss-Seidel iterative process (k indicates the actual iteration), fulfilling the complementarity conditions, until the residue in the discrete Elrod-Adams equation (11) reaches a certain tolerance.

$h(x_1, x_2, t)$ is also an unknown that must be acquired solving the ring dynamic. It is computed using equation (9), while $Z(t)$ is approximated by the Newmark scheme:

$$Z^n = Z^{n-1} + \Delta t U^{n-1} + \frac{\Delta t^2}{2m}(W^a(t_n) + W^h(t_n)), \quad (14)$$

$$U^n = U^{n-1} + \frac{\Delta t}{m}(W^a(t_n) + W^h(t_n)) \quad (15)$$

The proposed algorithm updates the dynamical variable $Z(t)$ simultaneously with the pressure and fluid fraction fields.

3.1 Multigrid acceleration

In Ausas et al. (2009a), a robust and efficient algorithm to solve dynamical lubrication problems with cavitation was presented. However, this algorithm is expensive from a computational point of view. A slow convergence on the long wave components of the pressure solutions is experienced while solving equation (2) in Ω_+.

Multigrid methods solve efficiently elliptic partial differential equations, particularly elliptic boundary-value problems (Fulton et al. (1986)), as in this case. The method is based in approximating a problem on multiple overlapping grids with widely varying mesh sizes and cycling between these approximations, using relaxation to reduce the error on each grid.

To solve this nonlinear elliptic boundary-value problem we employ the *Full Approximation Scheme*-FAS (Fulton et al. (1986)), which is based in solving for q^H the following fixed point problem:

$$\mathcal{N}^H(q^H) = r^H = I_h^H(\mathcal{R}^h(q^h, r^h)) + \mathcal{N}^H(I_h^H q^h), \tag{16}$$

where the discrete operator $\mathcal{N}^H$ is the left hand side of equation (11), r^H its right hand side and $\mathcal{R}^H$ its residue. $I_{h_1}^{h_2}$ transfers variables from mesh h_1 to mesh h_2. Superscripts (or subscripts) H and h indicate whether these are being computed on the coarse or the finer meshes.

Afterwards q^H is transferred to the finer mesh, adding the short-wavelength components:

$$\tilde{q}^h = I_H^h q^H + (q^h - I_H^h I_h^H q^h) \tag{17}$$

This new approximation $\tilde{q}^h$ contains less error in the long wavelength components, and therefore converges faster in the finest mesh. The operation $q^h \longrightarrow q^H \longrightarrow \tilde{q}^h$ is called a V-cycle.

3.2 The cavitation boundary issue with the mesh transfer operators

The major drawback of the multigrid method with the Elrod-Adams model is the shifting of the cavitation boundary done in the coarsest meshes. This situation is depicted in figure 2: a ring sliding on a untextured liner generates a pressure field Ω_+ (part of the domain with $\theta = 1$) is shown in the upper left corner. A zoom showing the finite volume centers occupies the upper right corner.

The position of the cavitation boundary changes when solved in the coarser meshes (fig. 2, bottom). The result is that the correction returned to the finest mesh will not resemble the problem solved in the finest mesh. Therefore the residue of equation (11) increases at the end of a V-cycle or at least stalls.

An effective strategy to solve this problem is maintaining the cavitation boundary position computed in the finest mesh. This is achieved by keeping the pressurized cells pressurized: if after a V-cycle the new value of pressure is null, the previous non-zero value is restored.

The definition of the mesh transfer operators I_h^H and I_H^h is also essential for a effective multigrid. It is to be noticed that the residue $\mathcal{R}^h(q^h, r^h)$ of equation (11) is the mass imbalance of the system. The *full weighting* operator Fulton et al. (1986) preserves this quantity, which was critical for an effective multigrid implementation.

The pseudo-code is given in algorithms 1 and 2.

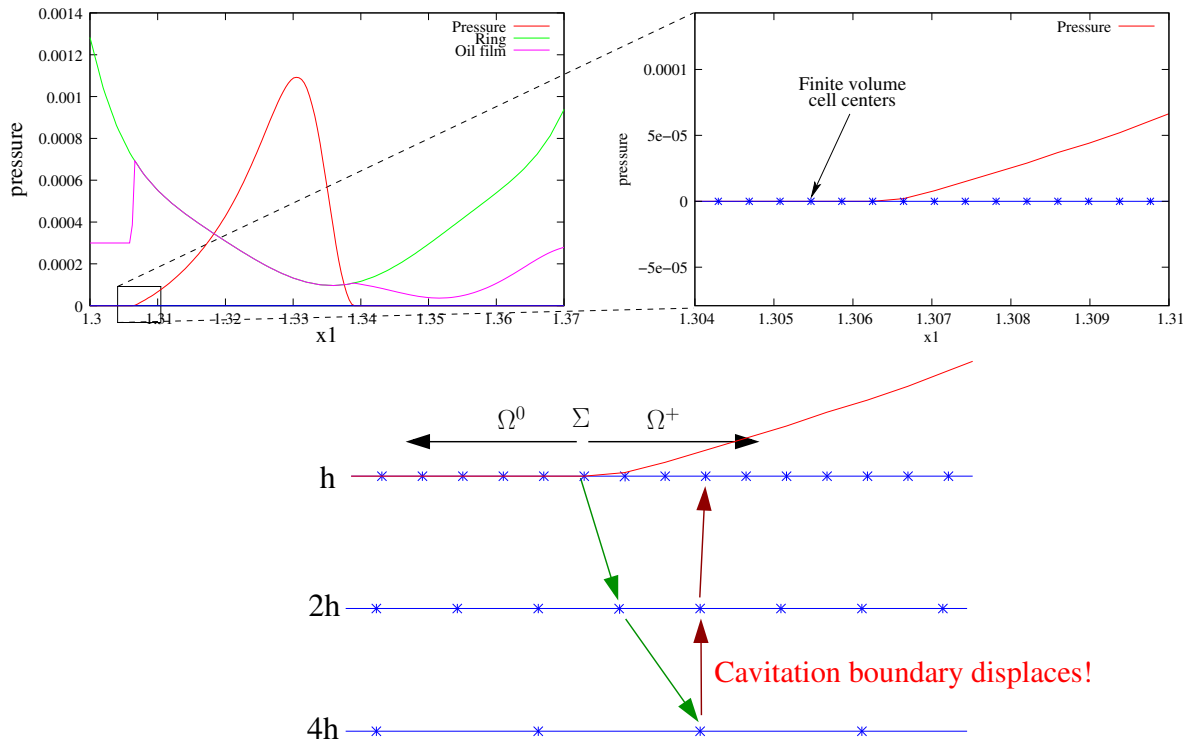

Figure 2: The cavitation boundary shift through a V-cycle.

Algorithm 1 Solving the Elrod-Adams equation coupled with dynamics

Set initial conditions $p^0_{i,j}$, $\theta^0_{i,j}$, Z^0, Z'^0
#Loop over time steps
for $n = 1 \rightarrow NT$ **do**
  $t_n = n\Delta t$
  $mesh = 0$ (start at the finest mesh)
  $p^{n-1}_{i,j} \leftarrow p^n_{i,j}$, $\theta^{n-1}_{i,j} \leftarrow \theta^n_{i,j}$, $Z^{n-1} \leftarrow Z^n$, $U^{n-1} \leftarrow U^n$
  while residue $>$ tolerance **do**
    Compute forces acting on the ring (W^a, eq. (10))
    Update $h(x_1, x_2, t)$ according to (9)
    Compute $RHS^h = 2\frac{\Delta x_1^2}{\Delta t} h^{n-1}_{i,j} \theta^{n-1}_{i,j}$
    $V - cycle(mesh, (p^{n-1}_{i,j}, \theta^{n-1}_{i,j}), RHS^h)$
    Check residue on eq. (11)
  end while
end for

Algorithm 2 $V - cycle(mesh, (p_{i,j}^{n-1}, \theta_{i,j}^{n-1}), r^h)$: a recursive routine

#Solving the problem in $mesh$
$relaxation(mesh, (p_{i,j}^{n-1}, \theta_{i,j}^{n-1}), \mathbf{r^h})$
if $mesh$! = coarsest mesh **then**
Compute the RHS of the problem solved in $mesh + 1$: $r^H = I_h^H r^h + I_h^H(r^h - N^h(r^h))$
#Descending in a V-cycle
$V - cycle(mesh + 1, (I_h^H p_{i,j}^{n-1}, I_h^H \theta_{i,j}^{n-1}), \mathbf{r^H})$
#Ascending...
Return the corrected value $\tilde{\mathbf{q}} = I_H^h \mathbf{q^H} + (\mathbf{q^h} - I_H^h I_h^H \mathbf{q^h})$ to $mesh$
Update p values without changing the cavitation boundary position in $mesh$
$relaxation(mesh, (p_{i,j}^{n-1}, \theta_{i,j}^{n-1}), \mathbf{r^h})$
end if

4 NUMERICAL TESTS

The importance of the conformity degree between the matching surfaces of a lubrified pair has been shown by Gadeschi et al. (2012) in numerical experiments involving textured rings (therefore steady state simulations) with a non mass-conserving algorithm. With this in mind the curvature radius of the ring R is varied in the interval $4 \leq R \leq 1024$. Typical values of R/L for barrel shaped compression rings are between 10 and 50. Notice that $R = 1024$ corresponds to a quasi conformal contact.

The assumed value of the ring mass per unit width $m_0 = 2 \times 10^{-5}$ corresponds to a dimensional value of 0.048 kg/m (with the chosen scales), which is realistic for the type of ring studied here. All simulations are computed with constant piston non-dimensional velocity $u = 1$. This matches mid-stroke velocity (where hydrodynamic lubrication can take place) for common diesel engines at high revolutions per minute. Furthermore, fully flooded conditions are addressed by setting d_{lub}= 20.

Besides the surface texture only the load on the pad remains to be determined, which is set at its lowest value to $W_0^a = 1.666 \times 10^{-4}$. A common non-dimensionalization in the tribology area is the Stribeck number:

$$S = \frac{\mu\, u}{W^a} = \frac{H^2}{6\, L^2}\, \frac{\hat{u}}{\hat{W}^a} \tag{18}$$

4.1 Multigrid performance

The multigrid speedup (quotient between the runtime without and with multigrid) is probably the most representative metric to measure its performance. In order to do so, we choose a representative texture composed of semi-ellipsoidal dimples (which will be defined in section 4.2.2) with parameters l= 0.05, d=10 and period λ= 0.2 (19.6% of textured surface). The ring curvature radius is R=64 while the load imposed on it leads to a Stribeck number of $S = 10^{-3}$.

Meshes of 512×32, 1024×64 and 2048×128 elements lead to cell sizes of 4, 2 and 1 microns. Courant number is fixed to 1, while 1000, 50 and 10 time steps are computed in each mesh respectively. Tolerance in the residue of equation (11) is set to 10^{-5} of the residue in the first relaxation at each time step (computed in the Euclidian norm). Enough relaxation sweeps/V-cycles are taken to achieve this precision, with up to 20 Gauss-Seidel iterations per multigrid level.

This test was carried out in a Intel Xeon 5430 machine (8 cores of up to 2.66 Ghz, 12 Mb of cache) with 32 Gb of RAM. The coarsest mesh used in every case was of 64×4 elements, thus giving 4, 5 and 6 meshes used in every V-cycle.

This is shown in table 1: execution times with Gauss-Seidel relaxation (column 1) and *FAS* (column 4) depict the benefits of the multigrid. The speedup grows with the problem size reaching the value 345.2 for the finest mesh, which is satisfactory for a highly nonlinear problem.

Mesh	Runtime without multigrid (s)	# of meshes in each V-cycle	Runtime with multigrid (s)	Multigrid speedup
512×32	30244	4	211	143.3
1024×64	4972	5	33	150.7
2048×128	20024	6	58	345.2

Table 1: Multigrid acceleration.

4.2 One and two-dimensional tests

The instantaneous non-dimensional *clearance* and *friction force per unit width* are given by:

$$C(t) \;=\; \min_{x_1,x_2} \; h(x_1,x_2,t)$$

and

$$F = \frac{1}{w}\int_0^w \int_a^b \left(\frac{\mu u\, g(\theta)}{h} + 3h\frac{\partial p}{\partial x_1} + 6p\frac{\partial h_L}{\partial x_1} \right)\, dx_1\, dx_2 \tag{19}$$

where the function $g(\theta)$ is taken as

$$g(\theta) \;=\; \theta\, s(\theta) \tag{20}$$

with $s(\theta)$ the switch function

$$s(\theta) = \left\{ \begin{array}{ll} 1 & \text{if } \theta > \theta_s \\ 0 & \text{otherwise} \end{array} \right. \tag{21}$$

In this friction model θ_s is a threshold for the onset of friction, interpreted as the minimum lubricant fraction needed for shear forces to be transmitted from one surface to the other. In all calculations the value $\theta_s = 0.95$ has been adopted. The friction coefficient then results from

$$f = \frac{H}{6L}\,\frac{F}{W^a} \tag{22}$$

where all quantities are non-dimensional.

Two quantities of interest are computed from the simulations, once the transients have passed and a periodic regime has been established. The *average friction coefficient* is related to power losses in engines

$$\overline{f} \;=\; \frac{1}{\frac{\lambda}{u}} \int_T^{T+\frac{\lambda}{u}} f(t)\, dt \tag{23}$$

while the *minimum clearance*

$$C_{\min} \;=\; \min_{T\le t\le T+\frac{\lambda}{u}} \; C(t) \tag{24}$$

is related to surface wear. As mentioned, T is large enough so that the periodic regime has been set.

4.2.1 One-dimensional textures

To study the effects of textures in the tribological performance of the lubrified pair, a sinusoidal texture is placed on the liner:

$$h_L(x_1,x_2) = d\,\frac{1 \,-\, \cos(2\,\pi\, x_1/\lambda)}{2} \tag{25}$$

Thus, the two parameters defining the surface are its period λ and the depth d. The ranges $0 \le \lambda \le 2$ and $0 \le d \le 10$ are explored with respective increases of 0.04 and 0.2 in each variable, leading to 2500 simulations for each ring curvature radius R, comprising a total of 5.000 transient simulations.

Every simulation is checked for spatial and time convergence: meshes of at least 512 ($\Delta x_1 \simeq 4 \times 10^{-3}$) and up to 4096 elements ($\Delta x_1 \simeq 5 \times 10^{-4}$) are chosen to ensure independence of spatial discretization. A Courant number of one is enforced.

It is interesting to see the texture's effect compared to that of an untextured liner maintaining the rest of the parameters. For that purpose we define:

- The relative variation V_f of the average friction factor:

$$V_f(d,\lambda) = \frac{\bar{f}(d,\lambda) - f_{\text{untextured}}}{f_{\text{untextured}}}$$

- The relative variation V_C of the minimal clearance:

$$V_C(d,\lambda) = \frac{C_{\min}(d,\lambda) - C_{\min,\text{untextured}}}{C_{\min,\text{untextured}}}$$

These variables are plotted in the $d-\lambda$ maps (figures) 3 and 4 for $m = m_0$.

The first map depicts the situation of a ring profile with $R = 32$, i.e. with a moderately pronounced convergent-divergent wedge, while the other one with a large curvature radius ($R = 256$) corresponds to an almost flat ring. This choice of R values is due to the fact that for the studied range of d and λ no reduction in friction nor increase in clearance was registered for $R \leq 16$.

Figure 3 shows the results for $R = 32$ and $W^a = 3W_0^a$. No increase in C_{min} is seen, as all V_C values in figure 3(b) are negative. Deeper textures lead to even lower clearances. Moreover, the highest V_C value is $V_C = 0$ at $d = 0$ which is the untextured case.

It is interesting to see that even in this context of lower clearances, considerable reductions can be obtained in friction, as seen in fig. 3(a).

The previously described situation for V_C at R=32 changes when the sliding surfaces are nearly parallel, as with $R = 256$. A widespread region with high $V_C > 0$ values has now appeared in figure 4(b). For every depth, a maximum in clearance is reached for λ approximately between $0.75 \leq \lambda \leq 1.1$. This is shown for every d by the full thick line in black crossing the chart. Clearances are increased up to 30%. These higher clearances are accompanied by a substantial improvement in friction, as expected. The same previous texture with $d = 5$ and λ=1 for $R = 256$ returns 58% less friction than the untextured liner.

These results can be explained in terms of the load carrying capacity of textures with a size of about the contact length. In figure 5 the ring position has been fixed for textures with d=5 and three periods: λ=1.0, 0.5 and 0.25. Two instants are shown: (i) when the trough of the texture with λ=1.0 is centered with the ring (figures 5(a) for R=32 and 5(b) for R=256) and (ii) when the crest of the texture with λ=1.0 is centered with the ring (figures 5(c), 5(d)). It is clear from the figure that each dimple works as a moving wedge, with a pressurized region moving along with it. The pressure peak, the pressurized region and therefore the load carrying capacity grow with the dimple's period until it is approximately of the size of the ring's length. This effect is more pronounced for high conformity bearings, as a flat surface provides limited load carrying capacity.

4.2.2 Two-dimensional textures

In this section we assess semi-ellipsoidal textures as portrayed in figure 6. This resembles more the ones produced by LST than the simplified one-dimensional textures of the preceding section. They are defined by a radius l (circular section in the x_1-x_2 plane) and a depth

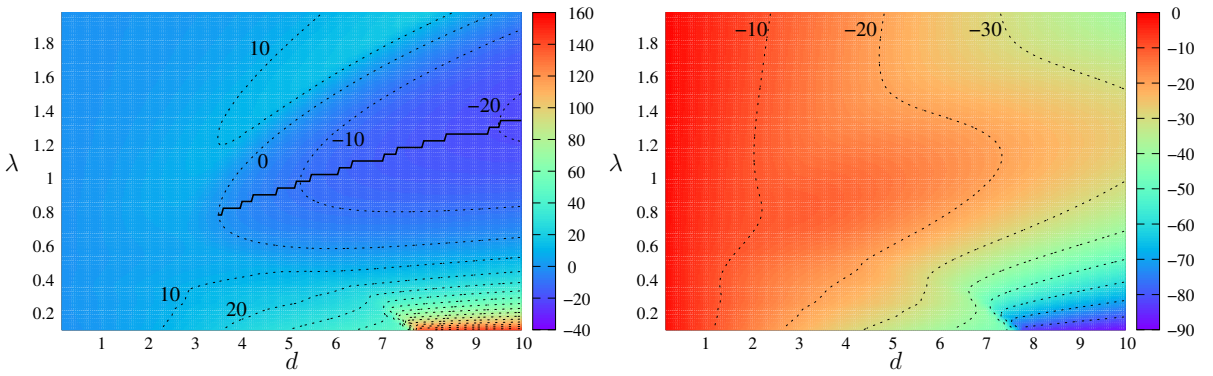

Figure 3: Relative differences for R=32 in (a) V_f and (b) V_C (expressed in percentages) with respect to the untextured liner, as functions of the texture parameters d and λ for a pad with $W^a = 3W_0^a$. The colorbars (as the isolines) indicate these percentages. The black line indicates the optimum λ for $d > 3$ in figure (a).

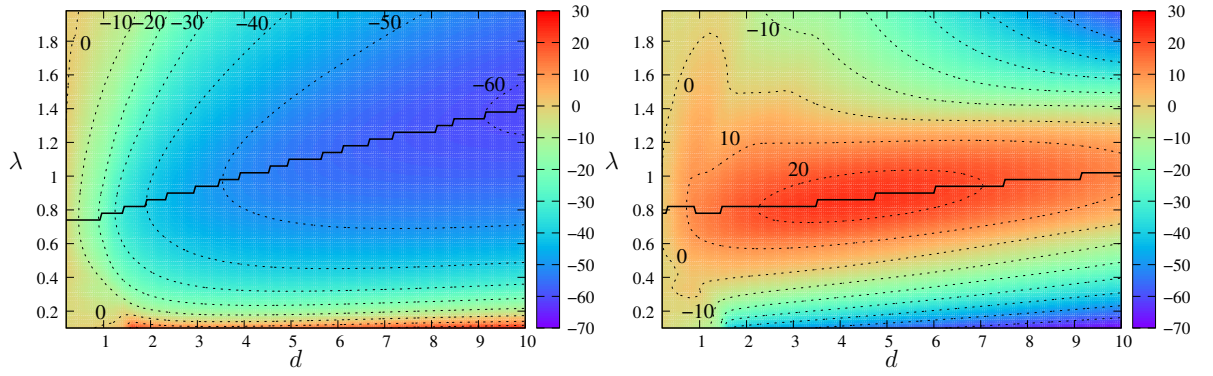

Figure 4: Same organization of results as in Fig. 3, but changing the curvature radius to $R = 256$. The black lines mark the optimum λ for every d.

d arranged in a square lattice of side λ. Notice that in this case textures are allowed to be "separated": a plateau is formed between dimples when $2l < \lambda$.

The texture parameters for the simulations in this section are chosen to be:

- l=0.01, 0.025, 0.05, 0.1 to 0.5 with increment of 0.1;
- λ=0.05, 0.1 to 1.0 with increment of 0.1;
- d= 2, 5, 10, 20 and 30.

The maximum dimple size is equal to the pad's length $\ell = L$. Excluding those cases not satisfying the thin film hypothesis ($l \leq 5d$) and non-overlapping of dimples ($2l \leq \lambda$) 112 different configurations remain. Again, $\overline{f}$ and C_{min} are extracted from the simulations once a periodicity has been established. Only one load $W^a = W_0^a$ on the ring is analyzed. Convergence (in time and space) was checked with 512×32, 1024×64 and 2048×128 meshes and a Courant number of 1.0. Computations are performed for 10 curvature radius yielding 1120 solved cases.

In figure 7 results are shown for the 1120 cases computed, each one represented by a small circle and organized by ring curvature radius R. The lowest friction coefficient of all computed

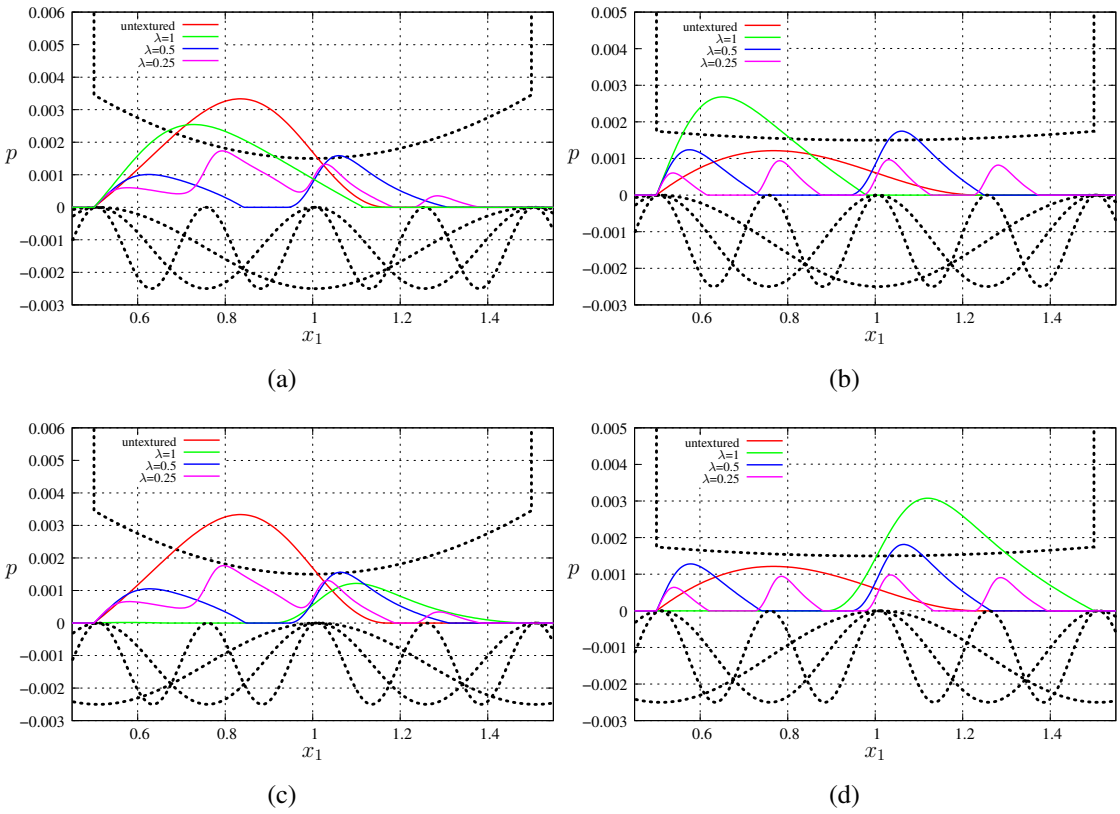

Figure 5: Pressure profiles with fixed ring position at $Z = 3.0$ for (a) R=32, t=0 ; (b) R=256, t=0; (c) R=32, t=0.5 ; (d) R=256, t=0.5. Notice that t=0 has been redefined as the instant at which the trough of the texture with λ=1.0 coincides with the ring centerline.

cases is 0.074 at R=4 and the highest clearance is C_{min}=6.4 at R=8. Both values correspond to the untextured liner. Improvements with texturing are achieved only for $R > 8$ in friction and $R > 16$ in clearance. For lower R values, no benefits over the untextured surface where obtained.

However, for sufficiently large R there are dimpled configurations that show enormous improvements over the untextured liner: up to 65% in friction and 75% in clearance. This is interesting since R/L ratios for compression rings are in the range 10-50 and are even higher for oil control rings (Gadeschi et al. (2012); Priest and Dowson (1999); Smith (2010)).

We now want to know which ones of the 112 dimpled arrangements returns the highest gains. The five textures with the best performance are listed in Table 2. The classification was made according to the distance to the best result (lower friction, higher clearance: the dotted lines in fig. 7) for each curvature radius R.

A clear trend is seen from the data of Table 2: λ, which is in all five cases is equal or approximately equal to 1.0 is also close or equal to $2l$. Those parameters represent a close-packed array of dimples of the size (or about the size) of the ring length ℓ. This is consistent with the results of the previous section. $\overline{f}$ and C_{min} for the texture with l=0.5, λ=1.0 and d=10 are highlighted in figures 7(a) and 7(b) with a red line.

5 CONCLUSIONS

In this work we have first addressed the problem of solving the piston/ring lubrication problem with the Elrod-Adams model. The robust mass-conserving finite volume algorithm pre-

(a) Best textures for large R							
$\overline{f}$				C_{min}			
#	l	λ	d	#	l	λ	d
1	0.5	1.0	10	1	0.5	1.0	10
2	0.4	1.0	10	2	0.4	0.9	10
3	0.5	1.0	20	3	0.4	0.8	5
4	0.5	1.0	5	4	0.3	0.7	5
5	0.4	0.8	5	5	0.4	0.9	5

Table 2: Best textures for large R values in terms of average friction coefficient and minimum clearance.

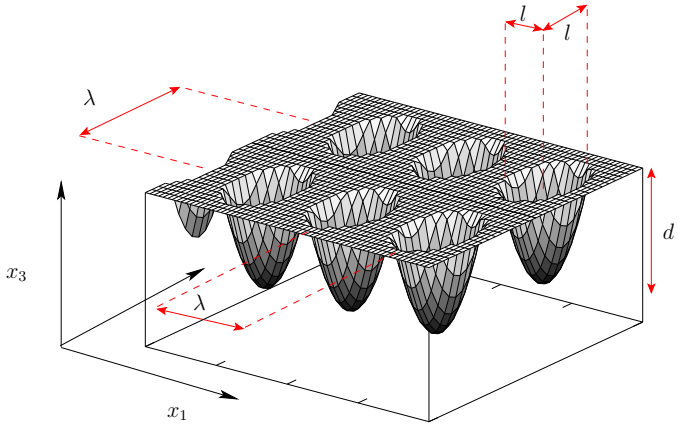

Figure 6: Pockets on the liner surface, resembling the ones produced with Laser Surface Texturing. λ, l and d are the texture's period, radius and depth.

sented in Ausas et al. (2009b) is modified to accelerate convergence by means of the *Full Approximation Scheme* (Fulton et al. (1986)). The shortcomings of a straightforward multigrid were studied and discussed, making emphasis on the problem of the shifting cavitation boundary. Solutions were offered for a efficient implementation.

Subsequently, the tribological effect of textured surfaces in the hydrodynamic regime was examined by virtue of extensive one and two-dimensional space and time converged numerical simulations. The piston velocity, oil viscosity and ring mass were chosen to mimic real engine cycle conditions at mid-stroke.

It was observed in both one and two-dimensional simulations that the ring profile determines whether texturing is beneficial or not. The performance of rings with moderate to high curvature radius (as is the situation of compression and more markedly oil control rings) is benefited by texturing. The more conformal the contact, the higher the gain, reaching reductions of up to 65% in friction. These gains decrease with the load as the mixed lubrication regime is approached.

In this context, the best textures for friction reduction and for maximizing ring/liner clearances are close-packed textures with a size of about the length of the ring. Two observations must be made: (a) this corresponds to an idealization, as tangent pockets (with thin walls between them) will render a surface prone to wear; and (b) all the results were obtained for specific conditions (hydrodynamic regime , constants piston velocity and load on the ring). For practical selection of liner textures the conditions (loads, velocities, oil feeding) along whole real engine cycle should be contemplated.

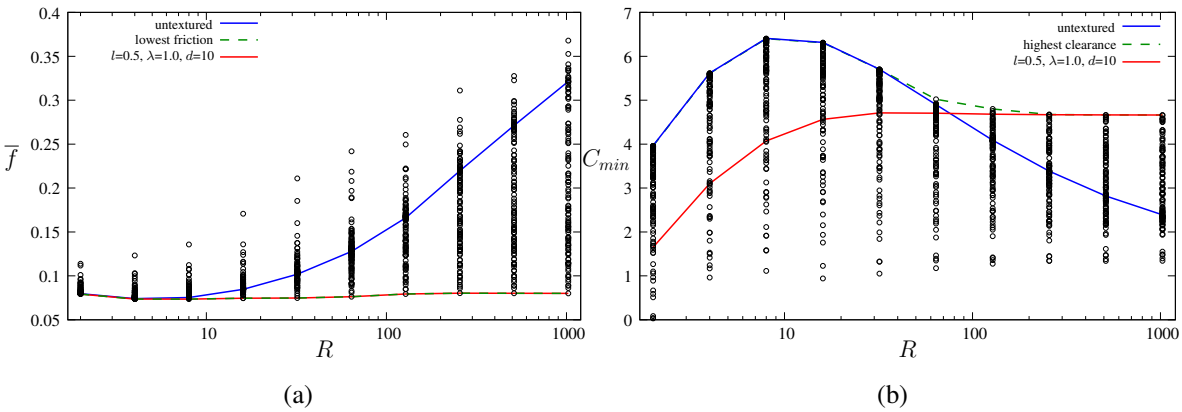

Figure 7: (a) Average friction coefficient $\overline{f}$ and (b) minimum clearance C_{min} for the 1120 two-dimensional cases computed. The two full lines link the circles of the results for (i) the dimpled surface of line 1 of Table 2 (in red) and (ii) the untextured surface (in blue). The dotted line in green connects the points with lowest friction (fig. (a)) and highest clearance (fig. (b)).

6 ACKNOWLEDGMENTS

The authors want to thank FAPESP (Fundação de Amparo À Pesquisa do Estado de São Paulo, Brazil, grants 2011/24147-5 and 2012/14481-8) and CNPq (Conselho Nacional de Desenvolvimento Científico e Tecnológico, Brazil, grant DS-8434433) for financial support.

REFERENCES

Ali F., Kř̆upka I., and Hartle M. Analytical and experimental investigation of friction of non-conformal point contacts under starved lubrication. *Meccanica*, 2012.

Ausas R., Jai M., and Buscaglia G. A Mass-Conserving Algorithm for Dynamical Lubrication Problems With Cavitation. *ASME Journal of Tribology*, 131:031702 (7 pages), 2009a.

Ausas R., Ragot P., Leiva J., Jai M. Bayada G., and Buscaglia G. The impact of the Cavitation model in the Analysis of Micro-Textured Lubricated Journal bearings. *ASME Journal of Tribology*, 129:868–875, 2009b.

Bifeng Y., Li X., Fu Y., and Yun W. Effect of laser textured dimples on the lubrication performance of cylinder liner in diesel engine. *Lubrication Science*, 24:293–312, 2012.

Buscaglia G., Jai M., Cadalen J.P., and Choukroun F. Mass–conserving numerical simulation of pisto ring/liner contact along a full engine cycle. *Mecánica Computacional*, XXIX:3257–3279, 2010.

Checo H., Ausas R., Jai M., Cadalen J.P., Choukroun F., and Buscaglia G. Moving textures: Simulation of a ring sliding on a textured liner. *Tribology International*, 72:131–142, 2014.

Cho M. and Park S. Micro CNC surface texturing on polyoxymethylene (POM) and its tribological performance in lubricated sliding. *Tribology International*, (44):859–867, 2011.

Costa H. and Hutchings I. Hydrodynamic lubrication of textured steel surfaces under reciprocating sliding conditions. *Tribology International*, 40:1227–1238, 2007.

Dobrica M., Fillon M., Pascovici M., and Cicone T. Optimizing surface texture for hydrodynamic lubricated contacs using a mass-conserving numerical approach. *Proc. IMechE*, 224:737–750, 2010.

Elrod H.G. and Adams M. A computer program for cavitation. Technical report 190. *1st LEEDS LYON Symposium on Cavitation and Related Phenomena in Lubrication, I.M.E.*, 103:354, 1974.

Etsion I. State of the art in laser surface texturing. *J, Tribol.: Trans. ASME*, 127:248–253, 2005.

Etsion I. and Sher E. Improving fuel efficiency with laser surface textured piston rings. *Tribology International*, 42:542–547, 2009.

Fulton S.R., Ciesielsky P.E., and Schubert W.H. Multigrid methods for elliptic problems: a review. *Mon. Wea. Rev.*, 114:943–959, 1986.

Gadeschi G.B., Backhaus K., and Knoll G. Numerical Analysis of Laser-Textured Piston-Rings in the Hydrodynamic Lubrication Regime. *Journal of Tribology*, 134:041702–1–041702–8, 2012.

Kovalchenko A., Ajayi O., Erdemir A., and Fenske G. Friction and wear behavior of laser textured surface under lubricated initial point contact. *Wear*, 271:1719–1725, 2011.

Kovalchenko A., Ajayi O., Erdemir A., Fenske G., and Etsion I. The effect of laser surface texturing on transitions in lubrication regimes during unidirectional sliding contacts. *Tribology International*, 38:219–225, 2005.

Mishra S.P. and Polycarpou A.A. Tribological studies of unpolished laser surface textures under starved lubrication conditions for use in air-conditioning and refrigeration compressors. *Tribology International*, 44:1890–1901, 2011.

Organisciak M. and Cavallaro G.L.A. Starved hydrodynamic lubrication of the piston ring cylinder liner contact: Preliminary study of the influence of surface texturing. *Tribology and Interface Engineering Series*, 48:573–583, 2005.

Pettersson U. and Jacobson S. Textured surfaces for improved lubrication at high pressure and low sliding speed of roller/piston in hydraulic motors. *Tribology International*, 40:355–359, 2007.

Priest M. and Dowson D.T.C.M. Predictive wear modelling of lubricated piston rings in a diesel engine. *Wear*, 231(1):89–101, 1999.

Qiu Y. and Khonsari M. Experimental investigation of tribological performance of laser textured stainless steel rings. *Tribology International*, 44:635–644, 2011.

Ramesh A., Akram W., Mishra S.P., Cannon A.H., Polycarpou A.A., and King W.P. Friction characteristics of microtextured surfaces under mixed and hydrodynamic lubrication. *Tribology International*, (57):170–176, 2013.

Smith E.H. Optimising the design of a piston-ring pack using DoE methods. *Tribology International*, 44:29–41, 2010.

Tomanik E. Friction and wear bench test of different engine liner surface finishes. *Tribology International*, 41:1032–1038, 2008.

Tomanik E. Modelling the hydrodynamic support of cylinder bore and piston rings with laser textured surfaces. *Tribology International*, 59:90–96, 2013.

Wang X., Adachi K., Otsuka K., and Kato K. Optimization of the surface texture for silicon carbide sliding in water. *Applied Surface Science*, 253:1282–1286, 2006.

Yuan S., Huang W., and Wang X. Orientation effects of micro-grooves on sliding surfaces. *Tribology International*, 44:1047–1054, 2011.

Zhang J. and Meng Y. Direct observation of cavitation phenomenon and hydrodynamic lubrication analysis of textured surfaces. *Tribology Letters*, 46:147–158, 2012.